Introduction to organic solar cells and components:

Fig. 1 shows an example of a flexible organic solar cells (OSC) used to convert sunlight to electricity. OSCs can be constructed to be thin, lightweight and flexible. As such, they are also easy to install. On the basis of these characteristics, organic solar cells have significant advantages over rigid, heavy and difficult to install silicon-based solar cells. Organic solar cells can be especially suitable in applications involving installations at the outsides of buildings and on the surfaces of complex shaped products, including vehicles, backpacks and tents.[1] Defense applications would have been a serious market for organic solar cells since they have the capability to be placed over the surfaces of military equipment. However, there are currently no commercially available organic solar cells and their potential is unfulfilled.
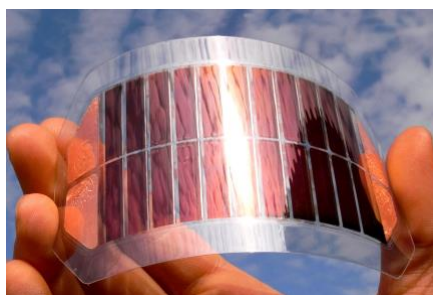

Figure S1. A flexible organic solar cell module.[2]

The typical design of an OSC is shown in Fig. 2, which involves an anode, a cathode and two layers consisting of an electron donor polymer and an electron acceptor small organic molecule.[3,4] During typical solar cell operation, photons excite electrons in the electron donor, leaving behind empty spaces in the highest occupied molecular orbital (HOMO) level, referred to as "holes". Excited electrons and holes are attracted to each other, constituting a tightly bound pair, i.e., the exciton. If the exciton can diffuse to the interface between the electron donor and electron acceptor layers before recombining, the exciton can dissociate by transferring the electron to the electron acceptor. Electrons (holes) then can travel through the electron acceptor (donor) to the cathode (anode) via charge hopping. Charge transfer is facilitated by a built-in electric field created by the different work functions of the anode and cathode.[5]
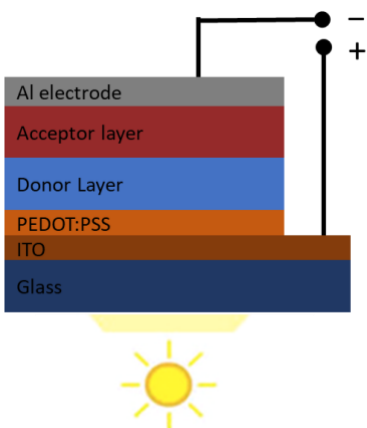

Figure S2. The layered design of an organic solar cell.

Another type of promising OSC is based on the bulk heterojunction design as shown in Fig. 3. In heterojunction cells the light-absorbing component is an active layer, i.e., a mixture, consisting of a conjugated polymer that is mixed intimately with an electronegative molecule, to constitute a nanostructured blend.[6] The physics of basic heterojunction device configurations have been investigated extensively.[6-9]
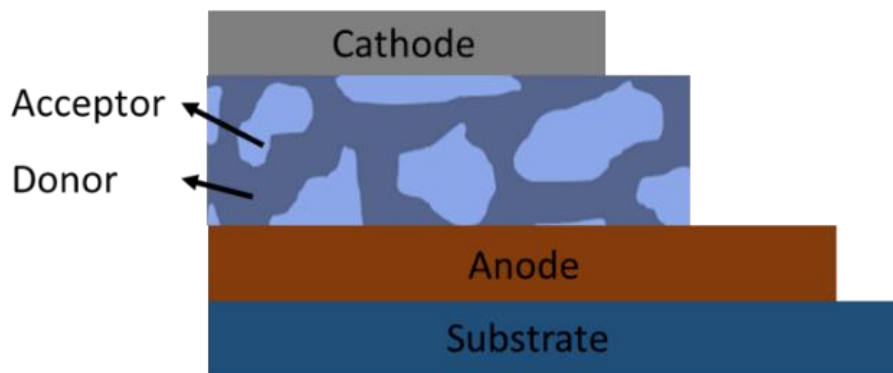

Figure S3. The modern bulk heterojunction cell design.

P3HT is a sulfur containing heterocyclic polymer, i.e., a polythiophene with a short alkyl group (hexyl, $CH_2(CH_2)_4CH_3$) on each repeat unit with a chemical formula of $(C_{10}H_{14}S)_n$. It is obtained via the polymerization of the monomer 3-hexylthiophene. The chemical structure is shown below:
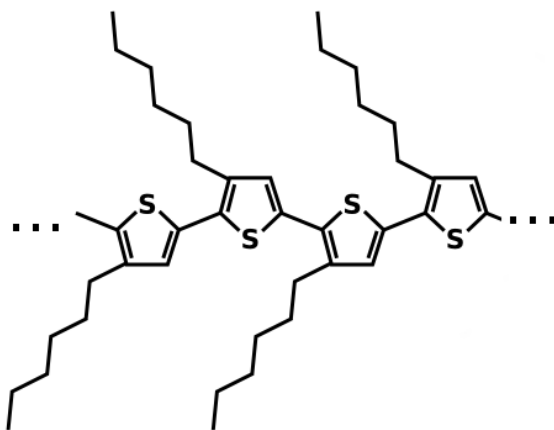

Figure S4. The chemical structure of poly(3-hexylthiophene) (P3HT).

P3HT can be found in two forms, regioregular P3HT (RR-P3HT) and regiorandom P3HT (RRa-P3HT), as shown below,[10] the difference is in the alternating positions of the alkyl chains along the backbone.
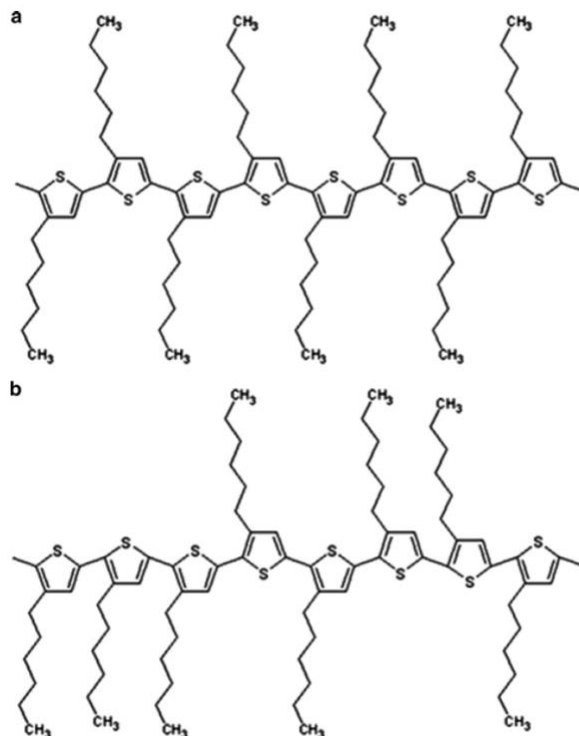
Figure S5. P3HT in the (a) regioregular form and (b) regiorandom form.

P3HT with regioregular structure can aggregate and crystallize via π (also called π-π stacking) interactions.[11-14] π-stacking occurs due to attractive, noncovalent interactions between aromatic rings, since they contain π bonds. The unit cell of RR-P3HT exhibits the unit cell dimensions of a=16.8 Å, b=3.8 Å and c=7.7 Å.[15] It has a density of 1,333 kg/m^3.[16] The crystal structure of RR-P3HT is shown below:[10]
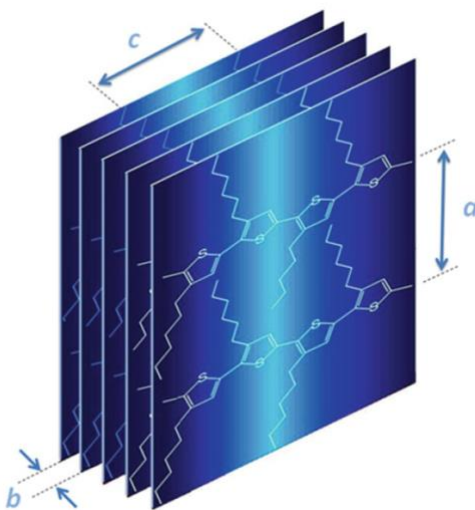

Figure S6. RR-P3HT in its crystalline form.

During the solution based fabrication of proto-type solar cells, RR-P3HT is dissolved in various solvents, including tetrahydrothiophene, chlorobenzene, 1,2-dichlorobenzene (o-DCB), o-xylene, with solubilities of 37.6, 15.9, 14.7, 2.7 mg/ml, respectively.[17] When dissolved, RR-P3HT is known to form colloidal particles in solution via crystallization. The formation of RR-P3HT colloidal particles and possibly crystalline nanofibers (also referred to as nanowhiskers) and their percolation, i.e., network formation via interactions with each other lead to the formation of volume-spanning networks. Such networks give rise to gelation, i.e., the formation of microgels, with junction points comprised of interacting crystal domains. Besides use in organic solar cells, RR-P3HT nanofibers have also been used for the fabrication of organic phototransistors (OPTs).[18]

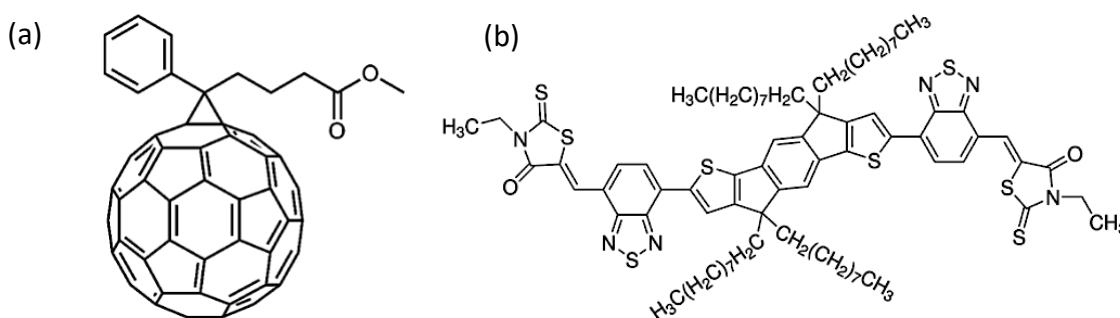The chemical structure of $PC_{60}BM$ and o-IDTBR is as follows:

Figure S7. The chemical structure of (a) $PC_{60}BM$. (b) o-IDTBR.

Twin screw extrusion and coating:

If the low viscosity and elasticity problem of the blends can be overcome there is great potential for the use of relatively cheap and scalable extrusion/coating based methods for the fabrication of the active layers of bulk heterojunction solar cells. A combination of twin screw extrusion and coating apparatus that is assembled in our laboratories is shown in Fig. 8.
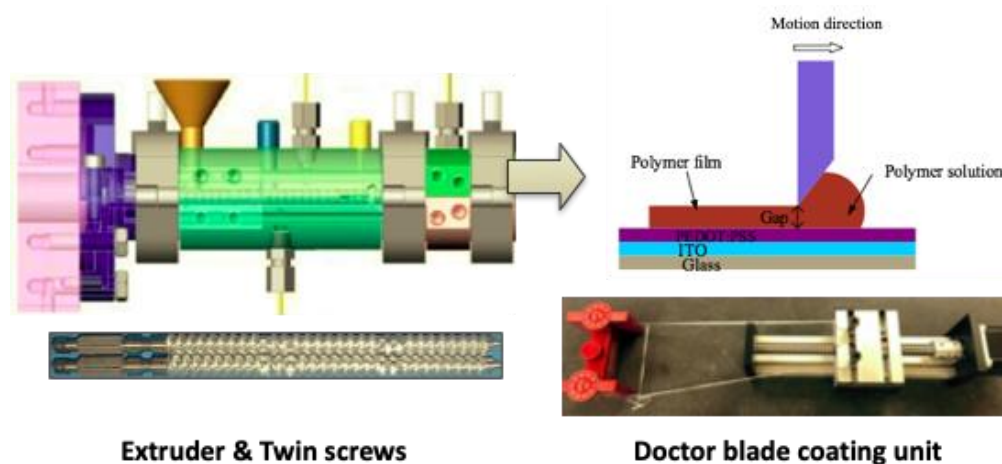

Figure S8. Twin screw extrusion slide with coating unit.

Rheological characterization equipment and methods:

Two sets of solutions in o-DCB and o-xylene were prepared and characterized. All rheological characterization experiments were carried out at a temperature of −5±0.2 °C which is the same temperature that was used earlier by He *et al.* in their experiments on P3HT/PC$_{60}$BM blends, the shearing of which under sub-ambient conditions provided benefits for increasing the conversion efficiency of photo-voltaic devices fabricated from P3HT/PC$_{60}$BM.[19]

An Advanced Rheometric Expansion System (ARES) rotational rheometer, available from TA Instruments of New Castle, DE was used in conjunction with a force rebalance transducer, 0.2K-FRTN1, and stainless steel parallel and cone and plate fixtures, all at a diameter of 8 mm. The cone angle was 0.1 rad. The torque accuracy of the transducer was ±0.02 g$_f$-cm. The actuator of the ARES is a DC servo motor with a shaft supported by an air bearing with an angular displacement range of 5×10^{-6} to 0.5 rad, and an angular frequency range of 1×10^{-5} to 100 rad/s. The ARES rheometer has an angular velocity range of 1×10^{-6} to 200 rad/s. The rheometer is equipped with an environmental control chamber, which can operate between −70 to 600 °C with a cooling and heating ramp rate that could be varied from 0.1 to 50 °C/min.

During the experiments at −5 °C, the zero gap (plates touch each other at the temperature of the experiment) was set first. The desired gap separation between the two discs was then imposed at the same temperature. Solutions were stirred on a hot plate at 70 °C, a predetermined volume was taken as a specimen (slightly greater than necessary to fill the gap) and via a pipette was transferred into the gap between the two discs and upon reaching the desired temperature the excess material was trimmed from the edge of the specimen. This process took about 1 min after the loading the specimen into the gap between the two discs. For each test, a fresh sample was loaded onto the rheometer to avoid any thermal and pre-shearing effects, unless indicated differently.

In steady torsional flow the apparent shear rate, $\dot{\gamma}_a$ (not corrected for slip effects), is given by, $\dot{\gamma}_a = \left(\Omega r / H\right)$, where r is the radial distance from the center of the disk, H is the gap height, and Ω is the angular velocity of the bottom plate. The shear stress at the edge of the disk, $\tau_w(R)$, can be determined from $\tau_w(R) = \frac{\Im}{2\pi R^3}\left(3 + \frac{dln\Im}{dln\dot{\gamma}_{\alpha R}}\right)$, where $\Im$ is the torque generated by rotating the bottom disk, $\dot{\gamma}_{\alpha R}$ is the apparent shear rate at the edge of the disk. If plots of apparent shear rate versus reciprocal gap are drawn at constant shear stress at the edge, the slopes would be equal to $2U_s$, where U_s is the slip velocity. The steady torsional flow experiments were carried out by systematically varying the surface to volume ratios via changes in the gap between the two parallel plates, i.e. 0.4, 0.8, and 1.2 mm.
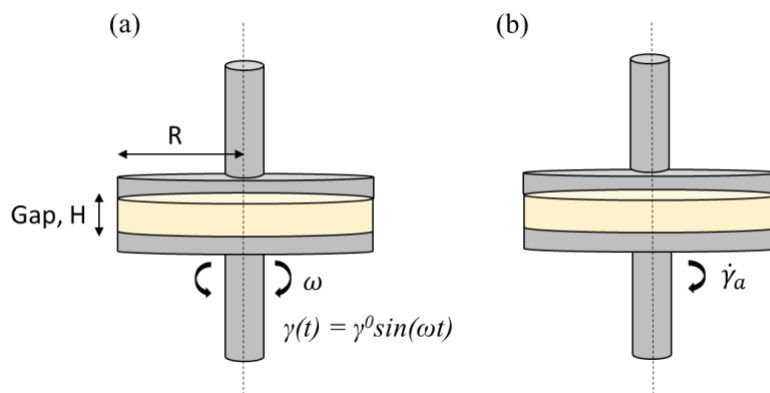
Figure S9. (a) Small-amplitude oscillatory shear. (b) Steady torsional shear.

Fig. S10 shows the time dependence of the storage modulus for the P3HT solution and the two P3HT blends, i.e., the P3HT:$PC_{60}BM$ and P3HT:o-IDTBR solutions at a constant P3HT concentration. It is interesting to note that the build-up of the nanocrystalline structure as reflected by the gelation dynamics occurs very differently for P3HT blended with $PC_{60}BM$ versus P3HT blended with o-IDTBR. There is no effect of the $PC_{60}BM$ on the rate of structure build-up of the P3HT blend (similar behavior was also noted in the He et al., 2019 study). However, for o-IDTBR the rate of gelation is initially higher, but the time to reach an equilibrium structure (and the ultimate gel strength) are smaller. It appears that the rates of aggregation and crystallization are higher for o-IDTBR but the ultimate crystallinity is lower, since crystallization ceases earlier.
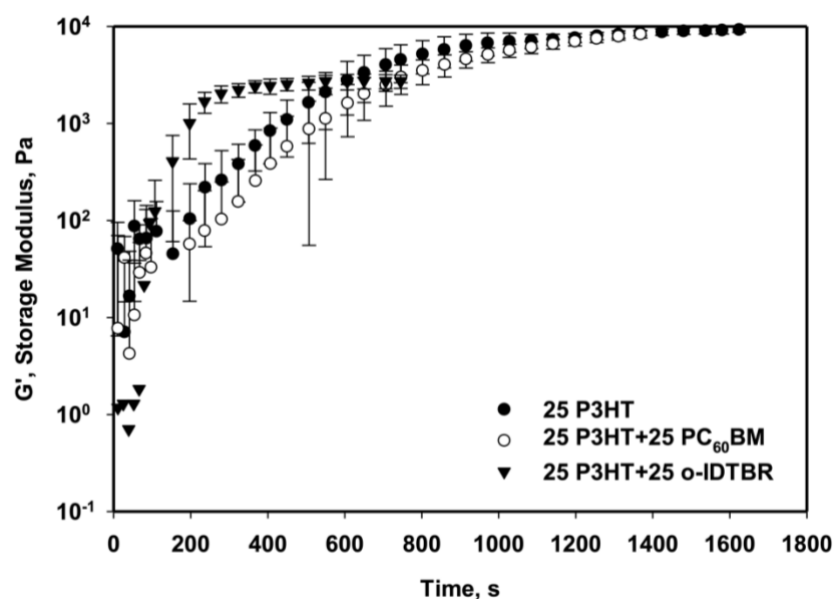

Figure S10. Storage modulus, G', versus time, t, of 25 mg/ml each for P3HT, P3HT and o-IDTBR, P3HT and $PC_{60}BM$ solutions in o-DCB upon rapid cooling to -5 °C.

Figure S11 shows the torque (and hence the shear stress) versus time during steady torsional flow for solutions of P3HT subjected to various apparent shear rates in the range of 10^{-3} to 1 s^{-1}.

Consistent with the steady torsional flow behavior of P3HT with PC$_{60}$BM solutions. The torque and hence the shear stress depends on the total strain that is imposed. The reduction of the shear stress (hence the torque, which is the integral of shear stress over the area of the disk fixture used in steady torsional flow) is indicative of the breakdown of the network of nanowiskers. It is interesting to note that the behavior appears to be different at the lowest apparent shear rates at which steady behavior is approached. The steady values of shear stress (torque) would be indicative of plug flow with the viscoplastic gel lubricated at the wall with an apparent wall slip layer.[20-24] This points to the importance of the wall boundary condition and the benefits that can be derived from maintaining a wall slip condition which would reduce the shear rate being imposed on the gel during a process like blade coating. The relationship between the structure of the gel and the rheological behavior is as significant as for example noted for hydrogen bonded complexes.[25]
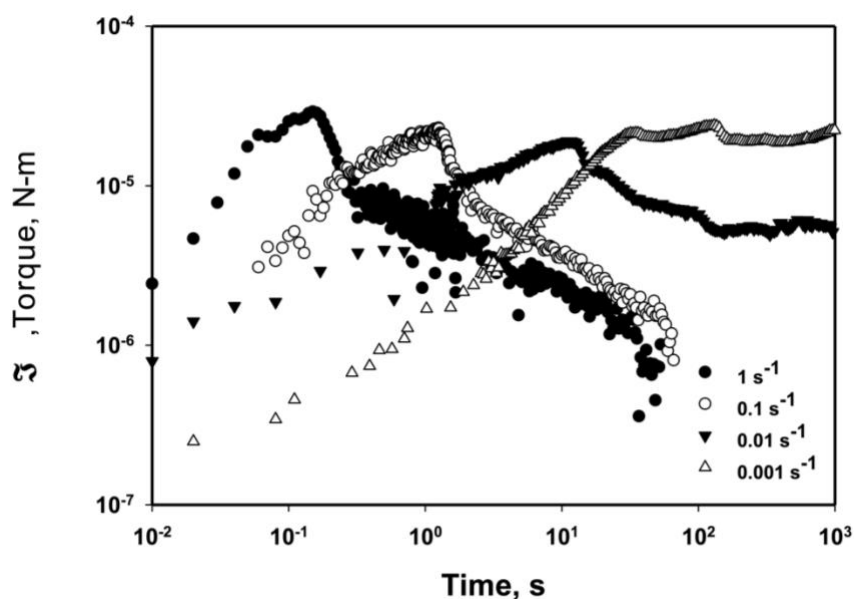

Figure S11. Steady-torsional tests torque, $\Im$, versus time, t, of 25 mg/ml P3HT solutions in o-DCB with apparent shear rates varying from 1, 0.1, 0.01 and 0.001 s-1 at −5 °C.

Differential scanning calorimetry (DSC)

Fig. S12 shows the DSC traces for pure P3HT versus P3HT blend with o-IDTBR. These traces are associated with the first heating of the specimens and thus reflect the effects of the thermo-mechanical histories that were imposed during the preparation of the solutions. Consistent with Fig. 11 the heating process at 10 °C/min is sufficiently slow to allow the crystallization of the o-IDTBR, which is reflected as the exotherm that is noted. The presence of o-IDTBR reduces the melting temperature (the highest temperature at which the last trace of crystallinity disappears) of P3HT.
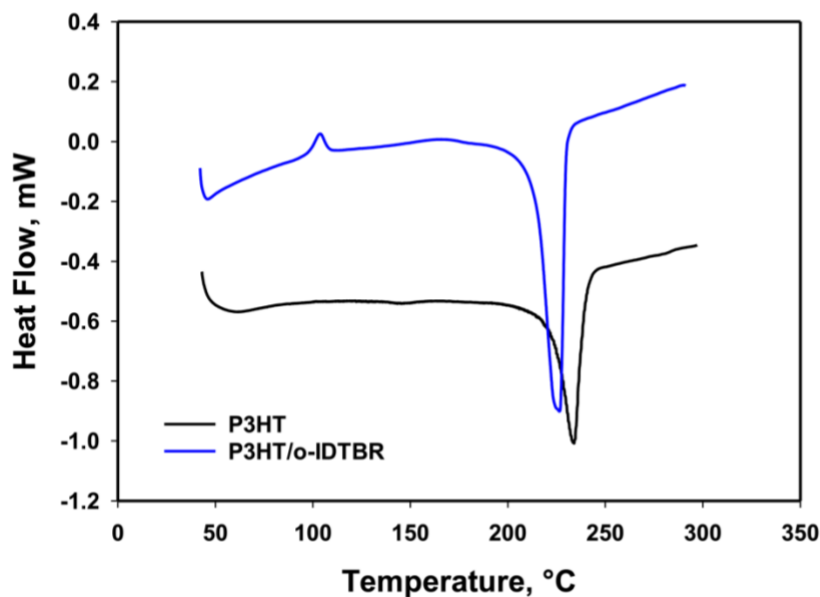
Figure S12. DSC first heating cycles of P3HT and 1:1 P3HT/o-IDTBR blend.

References

1   M. Jacoby, *Chem. Eng. News,* 2016, 94(18): 30-35.
2   https://www.ecofriendlylink.com/blog/organic-solar-cells.
3   D. Wöhrle and D. Meissner. *Advanced Materials,* 1991, 3(3): 129-138.
4   S. Günes, H. Neugebauer and N. S. Sariciftci. *Chemical reviews,* 2007, 107(4): 1324-1338.
5   A. M. Bagher, M. M. A. Vahid and M. Mohsen. *American Journal of optics and Photonics,* 2015, 3(5): 94-113.
6   A. Gusain, R. Faria and P. Miranda, *Frontiers in chemistry*, 2019, 7: 61.
7   C. J. Brabec, N. S. Sariciftci and J. C. Hummelen, *Advanced functional materials,* 2001, 11(1): 15-26.
8   E. Bundgaard and F. C. Krebs, *Solar Energy Materials and Solar Cells,* 2007, 91(11): 954-985.
9   D. Chen, A. Nakahara, D. Wei, D. Nordlund, and T. P. Russell, *Nano letters,* 2011, 11(2): 561-567.
10 M. Giulianini and N. Motta. *Springer,* New York, NY, 2012: 1-72.
11 M. Bernardi, M. Giulianini and J C. Grossman. *ACS nano,* 2010, 4(11): 6599-6606.
12 M. Aryal, K. Trivedi and W. Hu. *ACS nano,* 2009, 3(10): 3085-3090.
13 J. Xiao, J. Shi, H. Liu, Y. Xu, S. Lv, Y. Luo, D. Li, Q. Meng, Y. Li, *Advanced Energy Materials,* 2015, 5(8): 1401943.
14 V. Skrypnychuk, N. Boulanger, V. Yu, M. Hilke, S. C. B. Mannsfeld, M. F. Toney, D. R. Barbero, *Advanced Functional Materials,* 2015, 25(5): 664-670.
15 M. Giulianini and N. Motta, *Self-Assembly of Nanostructures. Springer, New York, NY,* 2012: 1-72.
16 Y. Sun, Y. C. Han and J. G. Liu. *Chinese Science Bulletin,* 2013, 58(22): 2767-2774.
17 N. Espinosa, M. Hösel, M. Jørgensen and F. C. Krebs, *Energy & Environmental Science,* 2014, 7(3): 855-866.
18 L. Persano, A. Camposeo and D. Pisignano, *Progress in polymer science,* 2015, 43: 48-95.
19 J. He, X. Kong, Y. Wang, M. Delaney, D. M. Kalyon and S. S. Lee, *ACS Applied Polymer Materials,* 2019, 1(3): 500-508.

20 B. K. Aral and D. M. Kalyon. *Journal of Rheology,* 1994, 38(4): 957-972.

21 D. M. Kalyon. *Journal of Rheology,* 2005, 49 (3): 621-640.

22 S. Aktas, D. M. Kalyon and B. M. Marín-Santibáñez and J. Pérez-González, *Journal of Rheology,* 2014, 58 (2): 513-535.

23 J. F. Ortega-Avila, J. Pérez-González, B M. Marín-Santibáñez, F. Rodríguez-González, S. Aktas, M. Malik and D. M. Kalyon, *Journal of Rheology,* 2016, 60 (3): 503-515.

24 E. F. Medina-Bañuelos, B M. Marín-Santibáñez and J. Pérez-González, M. Malik and D. M. Kalyon, *Journal of Rheology,* 2017, 61(5): 1007-1022.

25 Y. Wang, S. Aktas, S. A. Sukhishvili and D. M. Kalyon, *Journal of Rheology*, 2017, 61 (6): 1103-1119.